Pattern-Directed Dewetting of Ultrathin Polymer Films

Amit Sehgal,* Vincent Ferreiro, Jack F. Douglas, Eric J. Amis, and
Alamgir Karim*

*Polymers Division, National Institute of Standards and Technology,
Gaithersburg, Maryland 20899*

We utilize chemically patterned substrates with arrays of progressively narrower stripes ($1-15\ \mu$m) to investigate the influence of pattern size on the morphology of ultrathin dewetting polystyrene films. The scale and orientation of the spinodal-like height fluctuations of the dewetting patterns are coupled to the imposed substrate chemical frequency, providing a powerful means of morphological control. Dewetting patterns are correlated to the substrate pattern period leading to the formation of droplet arrays. The measurements confirm recent numerical simulations by Kargupta and Sharma of the existence of upper and lower cutoff scales for pattern recognition of a dewetting fluid. For pattern dimensions less than the characteristic scale on nonpatterned substrates, the droplets become anisotropic as they coarsen to a scale comparable to the stripe width, and then undergo a morphological transition to circular droplets that cross multiple stripes. This leads to quantization of droplet size and contact angles, as indicated by theory.

1. Introduction

Instabilities[1−7] at the deformable fluid−air interface in thin polymer films make the film structure sensitive to perturbations by substrate heterogeneities. These instabilities, though a source of difficulty in many applications, may also serve as a means of controlling film morphology. Dewetting[7−10] and phase separation[10−14] are attractive self-organizational processes for guiding these instabilities to form structures from nanometer to micrometer scale. This method of structuring polymer films has applications ranging from microfluidics to cell adhesion. Previous work has shown guidance of phase separation by substrate chemical patterns[10−12] and the coupling of surface deformation modes of spinodal decomposition to the underlying chemical pattern period.[13,14] The mathematical analogy[1,2,15] between phase separation and dewetting in thin polymer films by capillary instability (spinodal dewetting) suggests that we may similarly control the dewet film structure of ultrathin homopolymer films by the coupling of height fluctuations with the spatial scale and frequency of an underlying chemical pattern. In this paper, we demonstrate this method as a means of controlling the morphology of dewetting polymer films.

Recent work points to the strong influence of surface heterogeneity on the dewetting of thin polymer films.[8−10,13,14] Higgins and Jones[8] investigated the role of nanoscale film topography on polymer dewetting by casting poly(methyl methacrylate) films on glass slides roughened directionally by rubbing, floating these templated films onto water, and then depositing them on smooth polystyrene films spun cast on Si substrates. They found anisotropic correlation in droplet positions of the final dewetted polymer films. Nisato et al.[13] interpreted droplet arrays in blend films ($h \leq 20$ nm) on chemical patterns as arising from capillary breakup of fluid "threads" forming on the stripe patterns. Others have shown that commensurability of scales between the imposed surface patterns and the intrinsic scales of pattern formation is an important criterion for pattern recognition. The significance of scale for good templating has been shown to be relevant for phase separation,[12,16] block-copolymer ordering,[10] and, at an even finer scale, by chain length for dewetting on nanocorrugated substrates.[9] Theoretical investigations have also addressed dewetting[17] and equilibrium wetting on chemically patterned substrates.[18,19] A hydrodynamic model by Kargupta and Sharma[17] explores the influence of periodic wetting and relatively nonwetting stripes on the dewet film structure. The simulated dewetting film faithfully tracked the patterns only when the periodicity was greater than the spinodal wavelength[20] on homogeneous substrates (λ_h) but less than an upper cutoff scale where dewetting initiated near the stripe boundary ($\sim 2\lambda_h$). For stripe widths beyond the upper cutoff for ultrathin films, dewetting occurred as from homogeneous substrates.[17] Lenz et al. predict morphological transitions (homogeneous, heterogeneous, and film states)[18] with increasing fluid channel volume on stripes. The fluid covers non-wetting regions when the fluid volume is increased beyond a critical value by a spontaneous "bulging instability".[19]

(1) Vrij, A. *Discuss. Faraday Soc.* **1966**, *42*, 23.
(2) Wyart, F. B.; Daillant, J. *Can. J. Phys.* **1990**, *68*, 1084−1088.
(3) Reiter, G. *Phys. Rev. Lett.* **1992**, *68*, 75−78.
(4) Sharma, A.; Reiter, G. *J. Colloid Interface Sci.* **1996**, *178*, 383−399.
(5) Reiter, G.; Sharma, A.; Casoli, A.; David, M. O.; Khanna, R.; Auroy, P. *Langmuir* **1999**, *15*, 2551−2558.
(6) Sharma, A.; Khanna, R. *J. Chem. Phys.* **1999**, *110*, 4929−4936.
(7) Xie, R.; Karim, A.; Douglas, J. F.; Han, C. C.; Weiss, R. A. *Phys. Rev. Lett.* **1998**, *81*, 1251−1254.
(8) Higgins, A. M.; Jones, R. A. L. *Nature* **2000**, *404*, 476−478.
(9) Rehse, P.; Wang, C.; Hund, M.; Geoghegan, M.; Magerle, R.; Krausch, G. *Eur. Phys. J. E* **2001**, *4*, 69−76.
(10) Rockford, L.; Liu, Y.; Mansky, P.; Russell, T. P.; Yoon, M.; Mochrie, S. G. J. *Phys. Rev. Lett.* **1999**, *82*, 2602−2605.
(11) Krausch, G.; Kramer, E. J.; Rafailovich, M. H.; Sokolov, J. *Appl. Phys. Lett.* **1994**, *64*, 2655−2657.
(12) Böltau, M.; Walheim, S.; Mlynek, J.; Krausch, G.; Steiner, U. *Nature* **1998**, *391*, 877−879.
(13) Nisato, G.; Ermi, B. D.; Douglas, J. F.; Karim, A. *Macromolecules* **1999**, *32*, 2356−2364.
(14) Ermi, B. D.; Nisato, G.; Douglas, J. F.; Rogers, J. A.; Karim, A. *Phys. Rev. Lett.* **1998**, *81*, 3900−3903.
(15) Wyart, F. B.; Martin, P.; Redon, C. *Langmuir* **1993**, *9*, 3682−3690.

(16) Karim, A.; Douglas, J. F.; Lee, B. P.; Glotzer, S. C.; Rogers, J. A.; Jackman, R. J.; Amis, E. J.; Whitesides, G. M. *Phys. Rev. E* **1998**, *57*, R6273−R6276.
(17) Kargupta, K.; Sharma, A. *Phys. Rev. Lett.* **2001**, *86*, 4536−4539.
(18) Lenz, P.; Lipowsky, R. *Phys. Rev. Lett.* **1998**, *80*, 1920−1923. Significantly, our fluid is viscoelastic nonvolatile PS which is only *relatively* more wetting on the −COOH stripes. Dewet droplets coalesce along the stripes as opposed to stripes of condensed H_2O.
(19) Gau, H.; Herminghaus, S.; Lenz, P.; Lipowsky, R. *Science* **1999**, *283*, 46−49.
(20) Spinodal wavelength is the initial dewetting scale (refs 1 and 7).

These simulations and theories are compared to our measurements.

In the present paper, we quantify the influence of pattern scale and frequency on the morphological evolution of dewetting patterns of thin polystyrene (PS) films on topographically smooth chemically patterned self-assembled monolayers (SAMs). Chemical test patterns are designed with a range of stripe widths from 1 to 15 μm on the same substrate. This novel high-throughput approach enables us to systematically explore how pattern size influences the dewet film structure while all other parameters (thickness, temperature, casting rate, etc.) are held fixed.

2. Experimental Methods

A. Sample Preparation. The chemical patterns were created by soft lithography[21] on vapor deposited gold substrates [100 and 300 Å of Au over 10 Å of Cr, on Si(100) wafers, 4 in. diameter, N type, Polishing Corp. of America].[22] The substrates have a root-mean-square roughness of 3.5 Å, as verified by atomic force microscopy (AFM). This roughness is comparable to the typical 2−3 Å value for bare Si. The preparation of a smooth Au substrate is critical for excluding any contribution from surface roughness to the dewetting process. Topographically smooth SAMs are obtained by conformal contact of a poly(dimethylsiloxane) stamp "inked" with 1-hexadecanethiol ($-CH_3$ end group) on to the Au surface (Figure 1a), which is then immersed into a saturated hexadecane solution of an equivalent-chain-length 16-mercaptohexadecanoic acid ($-COOH$ end group). The 1-hexadecanethiol (92% mass fraction, CAS No. 2917-26-2, Cat. No. H763-7), the 16-mercaptohexadecanoic acid (90% mass fraction, CAS No. 69839-68-5, Cat. No. 44830-3), and the hexadecane (99%+ mass fraction, anhydrous) used in the microcontact printing were all purchased from Aldrich. The stamp is designed with multiple regions or bands with the linear pattern scale being varied systematically across the PDMS surface. The stamp geometry is illustrated in Figure 1b. The optical image at 200× and the three-dimensional AFM images below highlight the 3 μm ridges separated by rectangular channels that vary in width from 15 μm to 1 μm across the stamp. There are regions with 1.5 μm channels and 3.5 μm plateaus (period 5 μm) elsewhere in the stamp (not shown). Microcontact printing thus results in substrates that have a range of $-COOH$ stripe widths from (1 to 15) μm, separated by constant width (3 μm) bands of $-CH_3$ terminated thiols. Ultrathin films of polystyrene (PS) ($M_r = 760$, standard, Cat. No. 32782-4, Aldrich[22]) on these SAM patterns dewet spontaneously after spin casting.

The presence of residual solvent is a matter of concern in thin polymer films. The annealing process was avoided by the choice of the low M_r PS because the alkanethiol monolayer pattern may not be stable at elevated temperatures. To check for the influence of solvent, we spun cast our films from two very different solvents. The observed phenomena were largely independent of the choice of solvent. The spin casting of PS from toluene and chloroform solutions, with PS mass fractions of 0.75% and 0.25%, results in films of 12 and 18 nm thickness, respectively. Film thickness was estimated by integration over the late stage droplet volumes determined from the AFM images. The thicker 35 nm films were obtained by spin coating from a 1% toluene solution at 1500 rpm. The thickness was determined with a Filmetrics F20 [22] UV−vis reflectance interferometer, and the sample was subsequently annealed at 45 °C.

B. Measurement Methods and Analysis. Optical microscope (OM) images were acquired on a Nikon Optiphot-2 microscope[22] with a Kodak ES 1.0 CCD camera[22] mounted on the trinocular head, and stored as 8 bit, 1024 × 1024 pixel² digitized gray scale data. AFM was conducted on a Digital Instruments Dimension 3100 Nanoscope III in the TappingMode.[22] TESP-DI Nanoprobe cantilevers with Si tips were used with a spring constant of 30 N m^{-1} and a radius of curvature = 10 nm. In this

(21) Kumar, A.; Whitesides, G. M. *Science* **1994**, *263*, 60−62.
(22) Certain equipment, instruments, or materials are identified to adequately specify experimental details. Such identification does not imply recommendation by the NIST.
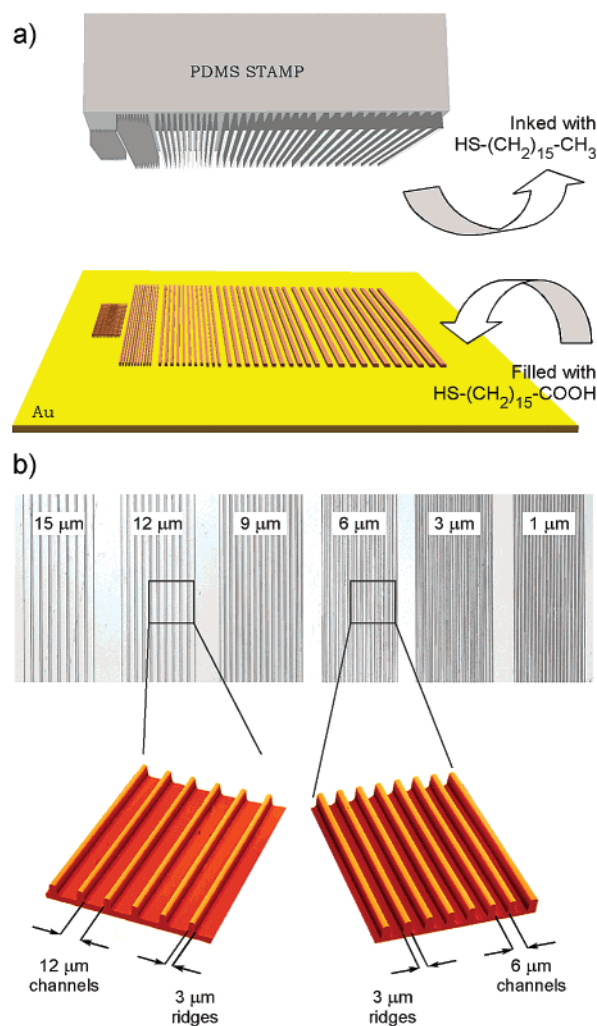

Figure 1. (a) Schematic of the microcontact printing method for generating topographically smooth SAMs. (b) Stamp geometry showing bands with discrete step variation of channel width from 15 to 1 μm while the 3 μm × 1 μm ridge dimension is held fixed. The 3-D AFM images highlight the asymmetric square wave periodicity with 1 μm high ridges.

mode "height" images are obtained as we raster an oscillating cantilever across the surface by a feedback loop that nominally keeps the displacement of the cantilever (the set-point amplitude, A_{sp}) from the surface constant. However, there may be small variations in this displacement with variations in the local interactions of the tip with a heterogeneous substrate. An engagement criterion of $A_{sp}/A_0 = 0.9$ was used, where A_0 is the free oscillation amplitude close to the resonance frequency. The vertical resolution of the atomic force microscope is <1 Å. The tip radius limits the lateral resolution. Scan frequencies of 0.5 Hz were used, giving 512 × 512 pixel² images. The scanned morphologies were verified to be independent of scan direction. AFM scans for droplets whose size is on the order of microns and maximum contact angles of 10° preclude concerns of errors in measurements due to tip shape or tip radius. These concerns are genuine only for measurements on the nanometer scale. A "planefit" filter was applied to all images prior to further analysis.[23]

Macros were developed and integrated in IGOR analysis routines for AFM data that automatically identify droplet positions and shapes and then generate vertical section profiles of all droplets along their major and minor axes. Differential analysis of the section profiles is then used to generate databases of maximal slopes (tangents) of the section profiles for all the droplets in the AFM height images (30−60 droplets) to generate

(23) DI "Dimension 3100 Scanning Probe Microscopes," Instruction Manual, Digital Instruments Inc., 2000.

contact angle data.[24] The AFM data were thresholded at known heights, generating cross-section areas of the droplets to determine particle size distributions, which were then corrected by the corresponding contact angles to generate the actual droplet sizes at the three-phase contact line. We thus generate distributions of droplet sizes and contact angles for AFM scans. These distributions reflect an intrinsic variability in the droplet morphology resulting from the dewetting process.

3. Results and Discussion

A. Dewetting Morphology Transition with Film Thickness. The stability of thin polymer films on surfaces and their deformation and rupture at the free boundary is determined by the effective interfacial potential (ϕ) between the polymer–air and the polymer–substrate interfaces.[2,3,5,6,25–27] Contributions from antagonistic short-range interactions and long-range van der Waals forces that generate potential profiles with minima at finite thickness result in instability whereby the excess free energy is minimized by a reduction in film thickness leading to rupture.[5,6,25,27] The range and magnitude of the long-range dispersion forces determine the thickness for onset of the various mechanisms of thin film breakup[5,6,25,27] to be either nucleated dewetting[3,26] (hole formation for thicker films) or metastable spinodal dewetting[7,27] for ultrathin films (typically <20 nm). Recently, simulations of Sharma et al. have studied the rupture of thin films on chemically heterogeneous substrates[28–30] and defined conditions for ideal templating[17] by the self-organization of thin films on substrates patterned with periodic wetting and nonwetting regions. Figure 2 presents experimental data highlighting the mechanisms for breakup and the typical dewetting patterns of thin PS films on chemically patterned surfaces. For a thicker film ($h = 35$ nm, Figure 2a), on a substrate patterned with 1.5 μm wetting stripes separated by 3.5 μm nonwetting regions, a nucleation-like mechanism results in the formation of holes distributed along the stripes. The hole formation or nucleated dewetting is distinct from our observation on thinner films ($h = 12$ nm, Figure 2b and c) that dewet by the formation of co-continuous patterns characteristic of spinodal dewetting. In spinodal dewetting, the film breakup proceeds by a capillary instability induced by thermal fluctuations in film height. The patterns in Figure 2b and c are reminiscent of spinodal dewetting of PS on homogeneous acid cleaned Si wafers,[7] but the proof of spinodal dewetting requires a full kinetic study as in ref 7. (Kargupta et al. also caution that the characteristic length scale of breakup on a periodic patterned substrate may be distinct from the spinodal wavelength on a homogeneous film.[17]) Though the morphological characteristics and our estimates (see Appendix) point to spinodal dewetting, we defer to the term "spinodal-like" in the absence of kinetic data for the evolution of the dewet structure. The films (Figure 2b and c) dewet spontaneously after spin casting, and evolve from optically smooth to the dewet structure shown, in 120 s after spin casting. The homogeneously distributed fluid threads in Figure 2b are characteristic of an intermediate stage of dewetting on a nonpatterned SAM. The presence
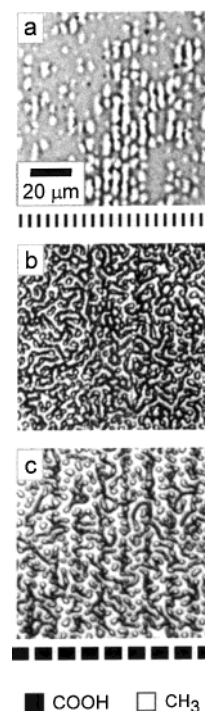

Figure 2. (a) OM image (96×96 μm^2) of a 35 nm thick film on SAM patterns. Breakup occurs by correlated hole formation along the stripes ($t = 20$ min, $T = 45$ °C). (b) Cocontinuous spinodal-like patterns formed on a nonpatterned SAM as film thickness is reduced ($h = 12$ nm, $t = 120$ s). (c) Spinodal-like patterns altered by the presence of a substrate chemical pattern. The dewetted surface structure tracks the underlying 9 μm vertical stripe pattern.

of an underlying linear chemical pattern (9 μm) is evident in Figure 2c from the optical contrast in the surface structure. Comparison of Figure 2c to Figure 2a illustrates the difference in the mechanism of breakup from spinodal-like to nucleated dewetting with film thickness. This paper demonstrates a coupling between the scale of the dewetting patterns and the substrate chemical periodicity of ultrathin films where breakup occurs by capillary instabilities.

Ideally AFM height data would be compared to the optical microscopy data presented here for the intermediate stages. However, the fast kinetics of the dewetting process precludes the use of AFM in the present system. The –CH$_3$ and the –COOH stripes are marked in Figure 2c. We believe that the difference in the polymer contact angles on the –CH$_3$ and the –COOH stripes may contribute to the contrast in the dewet morphologies, which fortuitously also enable us to visualize the pattern periods. The PS droplets appear to be darker where they have a higher contact angle (on the –CH$_3$ regions), and they are more spread out on the –COOH regions. It is also observable that thinner polymer threads and smaller droplets appear darker, as we only visualize the edges. The contact angles and optical appearance were verified on homogeneous –CH$_3$ and –COOH end-group SAMs where the droplets were found to spread more on the higher surface energy –COOH terminated SAMs. The complex structure and the appearance in the intermediate stages may however be misleading (The reader is referred to ref 17, Figure 5, and other works by the same authors[31]). These show that, for larger widths of the nonwetting regions, dewetting rates may be higher at the stripe

(24) Kerle, T.; Cohen, S. R.; Klein, J. *Langmuir* **1997**, *13*, 6360–6362.

(25) Sharma, A.; Khanna, R. *Phys. Rev. Lett.* **1998**, *81*, 3463–3466.

(26) Reiter, G. *Langmuir* **1993**, *9*, 1344–1351.

(27) Seemann, R.; Herminghaus, S.; Jacobs, K. *Phys. Rev. Lett.* **2001**, *86*, 5534–5537.

(28) Konnur, R.; Kargupta, K.; Sharma, A. *Phys. Rev. Lett.* **2000**, *84*, 931–934.

(29) Kargupta, K.; Konnur, R.; Sharma, A. *Langmuir* **2000**, *16*, 10243–10253.

(30) Kargupta, K.; Konnur, R.; Sharma, A. *Langmuir* **2001**, *17*, 1294–1305.

(31) Kargupta, K.; Sharma, A. *J. Colloid Interface Sci.* **2002**, *245*, 99–115.

boundaries, causing the evolving *intermediate* structure to evidence strips or droplets of polymer to get pinned in the center of the nonwetting regions. The final droplet structure evolves (shown subsequently in Figures 8 and 9) to a state having the droplets assembling on the wetting −COOH region.

B. Coupling of Dewetting Morphology to Substrate Patterns. Figure 3 (OM) illustrates intermediate stage dewetting of a 12 nm PS film on a patterned surface, 120 s after casting. The dewetting patterns are spinodal-like, yet reflect the dimensions and symmetry of the underlying SAM patterns. The substrate design with a discrete step-variation in the width of periodic chemical patterns across the surface allows simultaneous measurement for the entire range of pattern dimensions in a single snapshot at a fixed point in time. The advantage of the "high-throughput" approach is that it allows for a rapid comparative screening of the influence of the scale of a symmetry-breaking chemical field on dewetting behavior. Subtle changes may be quantifiably tracked across a sample where critical experimental parameters such as the film thickness, the underlying SAM layer, and the conditions for preparation and measurement are identical. Artifacts and errors in measurements in correlating multiple experiments are largely eliminated. Higher magnification (Figure 3a inset) shows the distinction between the dewet structures of the patterned (9 μm) and nonpatterned regions, with the *y*-axis defined parallel to the chemical patterns. It is apparent from Figure 3a that the orientation of the dewetting pattern becomes increasingly correlated with the SAM pattern as the pattern scale becomes finer. Fast Fourier transforms (FFT) quantify this progressive anisotropy with confinement (Figure 3b−e). The FFTs are characterized by a "spinodal ring" or "halo", which reflects the finer scale contribution from the wavelength and the orientation of the dewetting patterns, with overlaid high-intensity Bragg-like spots. The influence of the substrate pattern dimension is evident for each of the distinct dewetting pattern scales, with the strong distortion of the "spinodal ring" for the 3 μm pattern indicating alignment. (Local alignment in the order parameter with confinement has been seen in the spinodal decomposition of a phase separating binary mixture in quasi-two-dimensional thin film geometry.[32]) FFTs in Figure 3 show that the spinodal-like dewetting patterns exhibit similar correlations induced by chemical confinement on an underlying finite width SAM pattern.

The maxima in the FFT intensity section profiles (10 pixel wide sector average) along the *y*- and *x*-axes ($q^*_{y,x}$) provide the wavelength ($\Lambda_{x,y} = 2\pi/q^*_{x,y}$) of height fluctuations parallel and orthogonal to the pattern. The intensity profiles were iteratively fit by a nonlinear Levenberg−Marquardt algorithm to the Lorentzian, $I(q) = a + b/[(q − q^*)^2 + c]$. The FFT show that the maximum "spinodal ring" intensity in the *x*-direction shifts to higher *q* with a decrease of pattern size (q^*_x shifts 500%, from 0.28 μm^{-1} for the 15 μm stripes to 1.49 μm^{-1} for the 3 μm stripes). The characteristic wavelength of the dewet structure along the stripe (*y*-axis) orthogonal to the pattern period also decreases with decreasing substrate chemical period (Figure 4, q^*_y shifts 45% from 0.75 to 1.2 μm^{-1} from 15 to 3 μm stripes). The isotropic ring for the nonpatterned −CH$_3$ region (Figures 3e and 4) corresponds to a scale of $\Lambda = 4.2$ μm. We introduce a simple measure of the pattern anisotropy ($\Omega = \Lambda_y/\Lambda_x$), as a form of orientational order parameter on linear patterns. Dewetting for 6 μm stripes is isotropic ($\Lambda_x = 5.8$ μm, $\Omega = 1.02$), as in the nonpatterned

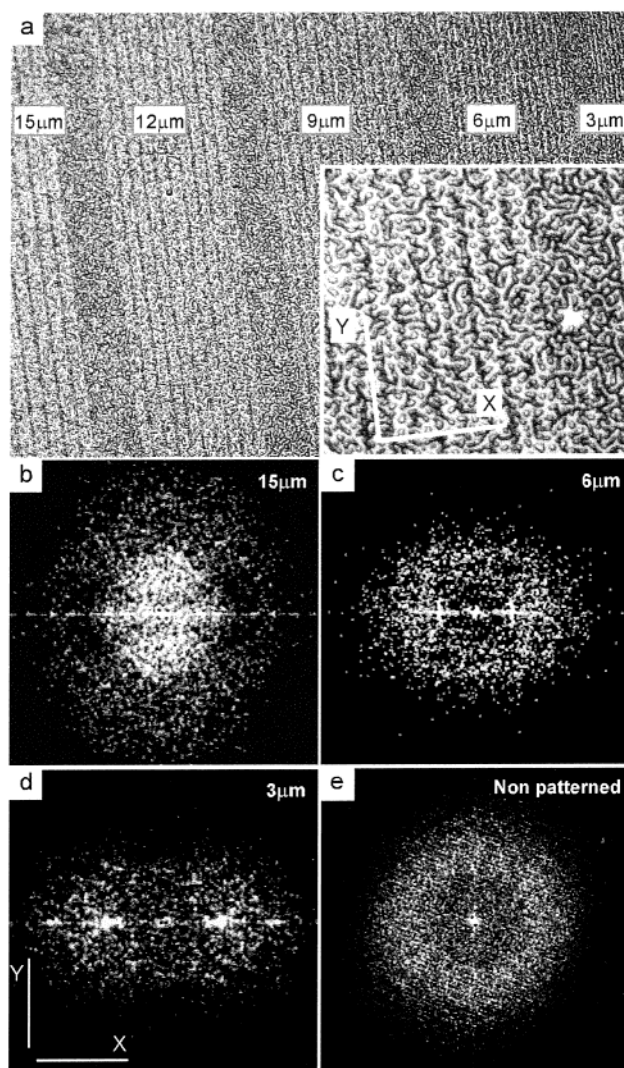(32) Tanaka, H.; Sigehuzi, T. *Phys. Rev. E* **1995**, *52*, 829−834.

Figure 3. (a) OM image of intermediate stage dewetting of PS on SAM patterns. The −COOH stripe width changes (15−3 μm) while the −CH$_3$ band is fixed at 3 μm. Inset: Magnification of the 9 μm stripe pattern. (b−d) FFT of patterned and (e) nonpatterned regions from the optical images.

case, becoming overtly anisotropic for 3 μm stripes ($\Lambda_x = 4.2$ μm, $\Omega = 1.34$). The anisotropy indicates alignment of the dewetting pattern with the confining substrate chemical field. Figure 5 quantifies the anisotropy, where Ω decreases with stripe width with a near linear dependence ($\Delta\Omega/\Delta$width $= −0.08$ μm^{-1}). The nearly straight-line dependence indicates that Λ_x is distinct from but closely coupled to Λ_y through the confining pattern dimensions. For values of $\Omega < 1$, the correlation length along the stripe, Λ_y, is less than Λ_x, as may be expected with increasing stripe width for height fluctuations of a fluid confined to a channel. This implies a transverse ($x-$) correlation of dewet structure for 12−15 μm stripes.

The substrate induces lateral height correlations along the *x*-axis that give rise to high-intensity Bragg spots (Figure 3b−d). These spots correspond to the extent to which the surface morphology recognizes the scale and symmetry of the SAM pattern. Figure 6a shows a 3-D representation of the FFT data for 12 μm stripes where the peaks rise sharply from a background "spinodal ring". The influence of pattern size on the FFT peaks is reflected in the set of intensity line profiles (averaged 5 pixel wide sectors) along the *x*-axis in Figure 6b. The background ring has been subtracted to give the Bragg components.
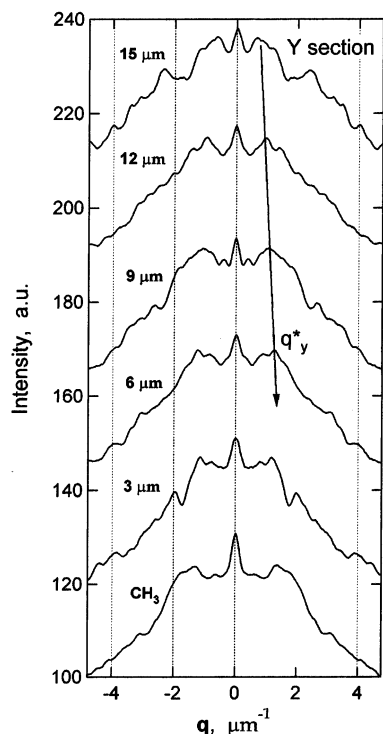
Figure 4. y-directional section profiles (10 pixel sector average) of the spinodal-like 2-D FFT rings for the patterns (15−3 μm) and the nonpatterned −CH$_3$ regions (offset for clarity). Reference OM images and FFTs are in Figure 3. The peak intensities (q_y*) shift to higher values with confinement.
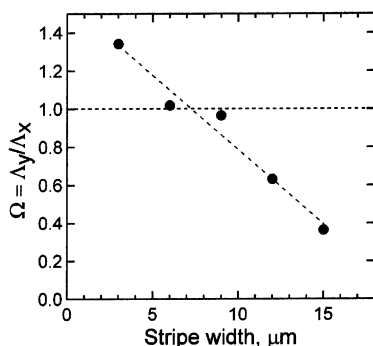

Figure 5. Dewet surface structure anisotropy ($\Omega = \Lambda_y/\Lambda_x$) with the confining stripe width. The dotted line ($\Omega = 1$) highlights nearly isotropic pattern scales for the 6 and 9 μm stripes.

Solid vertical lines and dotted lines, respectively, denote the fundamental spatial frequencies[33] ($q_1 = 2\pi/\lambda$, λ (μm) $= 15 + 3$, $12 + 3$, ...) and the higher order harmonics (q_n, $n = 2, 3, ...$) of the SAM patterns. The Bragg peak positions correlate strongly with the harmonics of the chemical pattern. This registry of the Bragg peaks with the underlying chemical frequency is also reflected in y- and x-sections of the spinodal-like ring. As an example, the sections for the 12 μm stripes are shown in Figure 6c with the reference Bragg peaks resolved along the zero line (data offset for clarity). Interestingly, we observe modulations in the y-section intensity profile of the ring that are correlated to Bragg peak positions along the x-axis, with the first maxima at one-half the pattern period (q_2). The modulations are also anticorrelated for the y- and x-sections. These correlations provide a measure of coupling
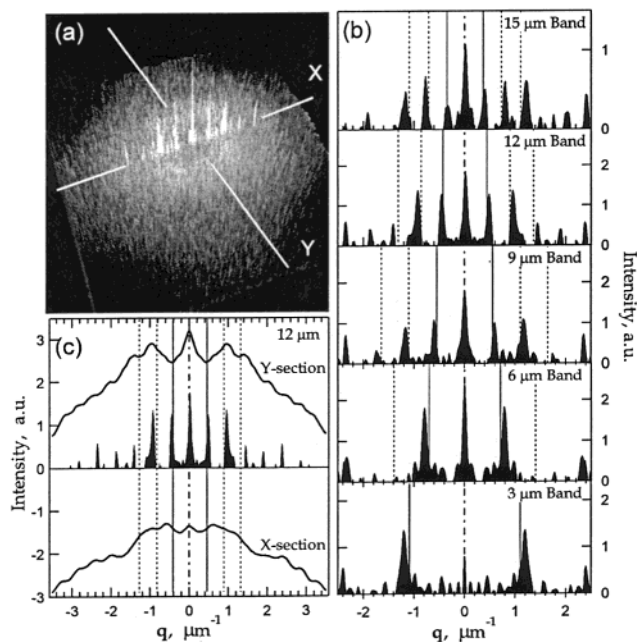

Figure 6. (a) 3-D representation of a FFT for 12 μm stripes highlighting Bragg-like peaks (x-axis) and the spinodal-like halo. (b) Power spectra of peak intensities from 2-D FFT data for patterns (15−3 μm) showing peak positions coincident with the harmonics of the substrate chemical spatial frequency (solid and dashed lines). (c) Spinodal-like ring sections for the 12 μm band (11 pixel wide average). Modulations in the y-section correlate to the Bragg peak positions. The FFTs and the Bragg peaks are resolved from the optical images shown in Figure 3.

between the quantized surface deformation modes of fluid in a strip[13,14] and the continuous spectrum of modes governing the initial dewetting stages. This hydrodynamic coupling allows us to exploit the scale and frequency of surface chemical patterns to control dewetting, as shown in former work for phase separation.[10,12−14,16]

C. Late Stage Droplet Coarsening on Stripes: Morphological Crossover. Film rupture is followed by Ostwald ripening or a diffusive coarsening process. The process must be modified for the constraint to coalesce quasi-one-dimensionally along the stripes.[34] As droplet size becomes comparable to the stripe width, the droplets must deform to avoid impinging on the nonwetting stripes. When the distortion becomes energetically unfavorable, the droplets return to a more symmetric shape, by *bridging* regions of unfavorable interaction.[18] Figures 7 and 9a show OM and AFM images of a late stage dewet film ($t = 120$ min) on the chemical test pattern. For larger (15−12 μm) stripes, we see droplet positions to be organized as "doublets" or two columns per band. As the pattern becomes narrower (9−3 μm), we observe a transition to arrays of confined single droplets that coalesce into registry with the underlying stripes. Further confinement to 6 μm stripes gives distorted (oval) droplets (Figures 8 and 9a) due to channel confinement into a single column along the band.[35] A loss of droplet alignment on the smallest pattern (1 and 1.5 μm) leads to a relatively "heterogeneous" morphology.[18] For the narrowest pattern (1.5 μm), we observe distorted ellipsoidal droplets with the major axis oriented along the y-axis (Figure 9a). The droplets are smaller and more confined for these narrower stripes.

(33) The power spectrum of alternate unit step-functions, of unequal widths α (COOH) and β (CH$_3$), was verified to be a Fourier series of periodicity $\alpha + \beta$.

(34) Correlation of interdroplet spacing along the y-axis to droplet size indicates 1-D coalescence. The y-spacing for larger droplets on 6 μm stripes (Figure 9a) is greater than that for smaller droplets on 1.5 or 12 μm stripes. The x-spacing of the droplets is however only governed by the confining pattern size.
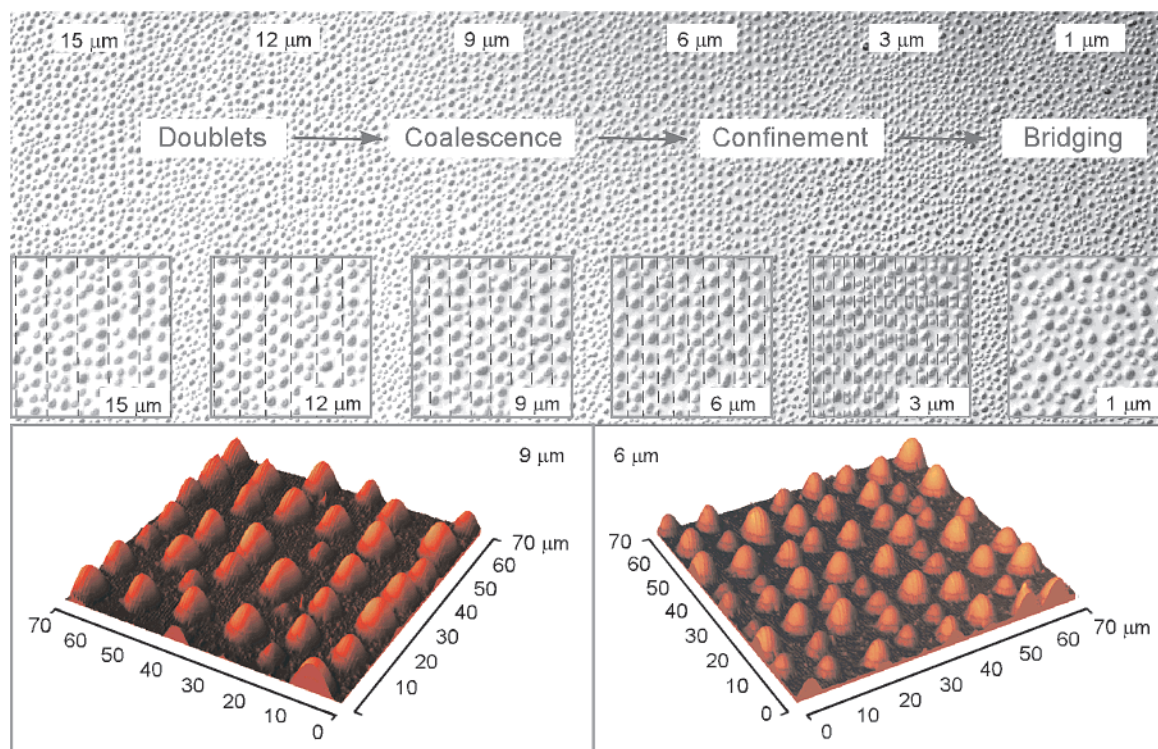
Figure 7. Library of the late stage morphology of the droplet arrays with pattern dimension. OM images and insets show transition from the doublet state (15−12 μm), to coalescence (9 μm), confinement (6 and 3 μm), and a heterogeneous morphology (1 μm) with bridging over multiple bands. Dashed lines (insets) indicate registry with the underlying chemical pattern period. AFM images (9 and 6 μm) highlight control of droplet size and spatial position.

When the anisotropy becomes sufficiently large, the larger droplets bridge across unfavorable −CH$_3$ bands to become more rounded. This spontaneous bridging transition is similar to the bulging transition observed by Gau et al. under near equilibrium conditions.[19] Figures 7 and 9a depict how the confining chemical pattern induces morphological evolution from droplet doublets, to their coalescence, and confinement to a "channel state"[18] and, finally, by droplet bridging, transitions to a disordered morphology.[18]

These morphological transitions verify the presence of upper and lower cutoff scales for templated self-organization of dewetting films on patterns. The isotropic ring for the nonpatterned −CH$_3$ region (Figure 3e) defines a measure of the lower cutoff scale,[17] $\Lambda = 4.2$ μm, with a predicted upper cutoff at approximately $2\Lambda = 8.5$ μm. The spinodal wavelength ($t \sim 0$) of the dewetting patterns on isotropic −COOH terminated SAMs is expected to be comparable to that of the −CH$_3$ regions. The theoretical framework and the simulations of Kargupta and Sharma[17] have indicated that the initial characteristic length scale (λ_h) of the dewetting on chemically heterogeneous patterned substrates (both −COOH and −CH$_3$ regions) is comparable to the spinodal wavelength (λ) on the *nonwetting regions* (−CH$_3$). PS dewets on both −CH$_3$ and −COOH terminated SAMs ($\lambda_h/\lambda \sim 1$; the chemical potential gradient $\Delta\phi$ is small). This wavelength for the nonwetting region hence formulated the basis for experimental design of the stamps and was used to merely serve as a measure

for estimating the upper and lower cutoff scales, as in the simulations. The simulations also show that the kinetic evolution and the final pinned structure are influenced by the periodicity and the relative width of each stripe. The figures indicate the lower cutoff scale (<3 μm stripes, period 6 μm) where for the 1.5 μm stripes the dewetted pattern does not follow the surface pattern (Figure 9a) and an upper cutoff (> 9 μm) where the 12 μm stripes droplet doublets are first observed. Significantly, the wavelength for the 6 μm patterns at this stage ($\Lambda_x = 5.8$ μm) is commensurate with the pattern size, but is greater than the lower cutoff scale required for faithful pattern recognition.[18] There is good pattern recognition in this intermediate regime: 9 μm ($\sim 2\Lambda$) to 3 μm ($\sim\Lambda$). The distorted confined droplets on the 3 μm stripes are unstable and lend to a heterogeneous morphology at later times. The commensurability of scales and the existence of upper and lower cutoff scales for pattern recognition accord well with simulations of Kargupta et al.[17]

Analysis of size and contact angle of dewet droplets yields insight into the influence of the confinement in the late stages. Particle analysis procedures (IGOR) applied to 80 × 80 μm^2 AFM images generate droplet cross-sectional areas, as outlined in Figure 8 for a dewet film on 6 μm chemical patterns. The height information in the AFM data is preserved, allowing for thresholding and calculation of the cross-sectional areas and perimeter at known heights for each droplet. Edge detection algorithms exclude particles at the perimeter of the scanned area from analysis. The section area is used to identify the coordinates of the areal 2-D center of mass for each droplet. Vertical section profiles through the center of mass of each droplet along the x- and y-axes, $P_y(x)$ and $P_x(y)$, respectively, are then used to determine droplet shape. Figure 8 shows the y-directional $P_x(y)$ through the center of mass for the nearly circular droplet numbered 28. The derivative of

---

(35) There may be a very fine difference in the displacement of the cantilever from the surface even at a constant set-point arising from the difference in the interaction of the tip with the local material properties in the tapping mode. The authors do observe a faint signature in Figures 8 and 9 for the thin −CH$_3$ terminated stripes, which possibly result from this difference in the interaction of the tip with the SAM. This enables us to clearly identify the droplets as assembling on the −COOH stripes.
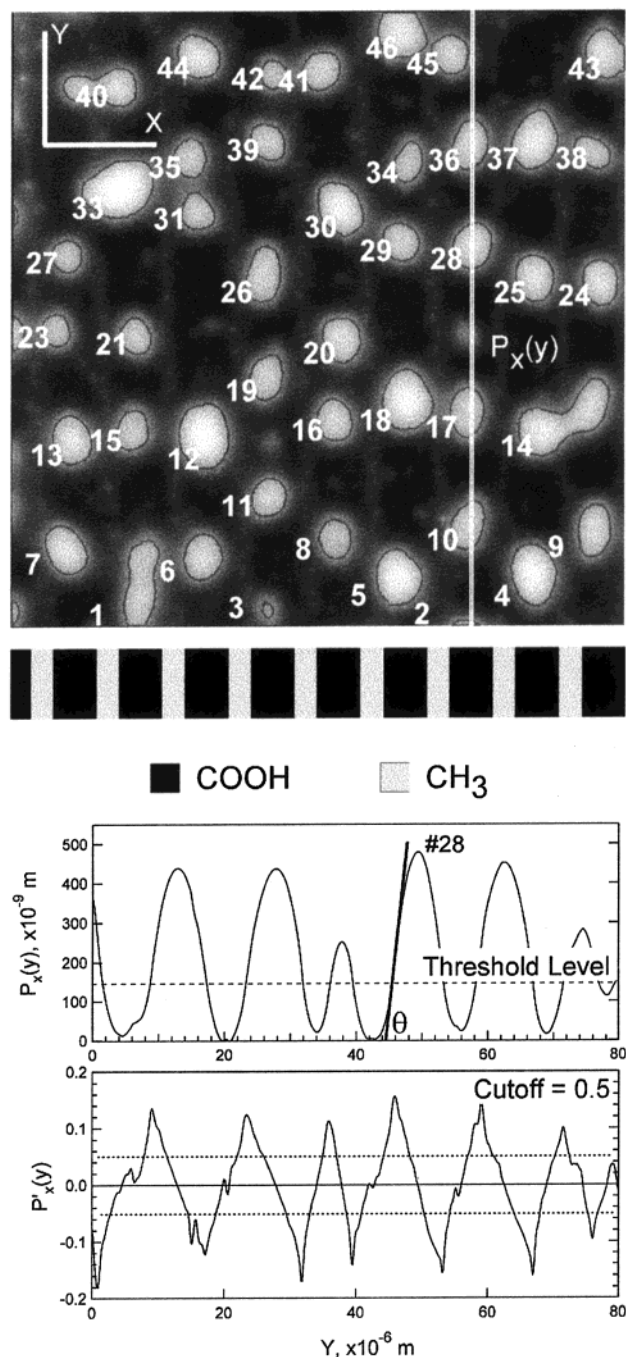
COOH   **CH₃**

Figure 8. Droplet structure analysis for an $80 \times 80 \ \mu\text{m}^2$ AFM scan for dewet droplets on the 6 μm substrate stripe pattern. The $-\text{CH}_3$ and the $-\text{COOH}$ terminated SAMs are clearly delineated. The image threshold is delineated by the outlines on each droplet. The vertical section profile at constant x-coordinate, $P_x(y)$, outlines the droplet shape and dimensions. $P'_x(y)$ gives the maximum and minimum slopes, which provides a measure of the contact angle, $\theta_y = \arctan[P'_x(y)]$.

the profile, $P'_x(y)$, for the droplet used with peak detection algorithms gives the maximal slopes across the droplet to be 0.149 and 0.152, which are a measure of the y-directional contact angles for the droplet. The thresholded sectional dimensions are then projected with known contact angles to determine the actual droplet dimensions. Automated procedures are used to generate databases of x- and y-directional droplet dimensions and contact angles for morphological characterization of all the AFM images.

     Below each AFM image (Figure 9), we show distribution of droplet sizes (D_x) and the dynamic contact angles[36] (θ_x)
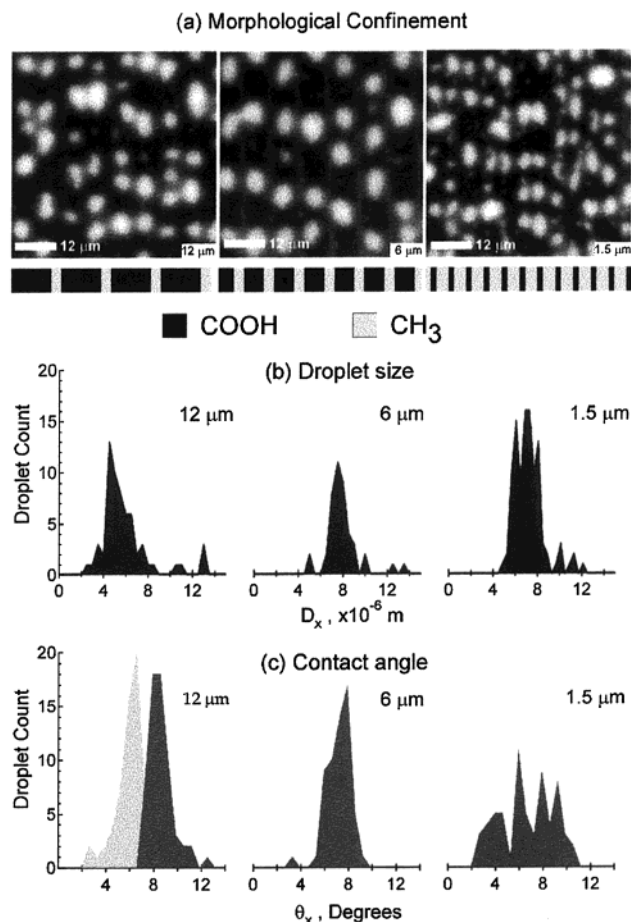

Figure 9. Effect of confinement (a) on distributions of droplet size (b) and contact angles (c). $60 \times 60 \ \mu\text{m}^2$ AFM scans (a) are shown for $-\text{COOH}$ stripe widths of 12, 6, and 1.5 μm. The substrate SAM patterns are shown to guide the eye. The data shown are the x-directional size and contact angle distributions, from section profiles $P_y(x)$ through the droplet centers of mass. Particle size and contact angle distributions are *quantized* on the 1.5 μm stripes.

measured along the x-axis. D_x peaks at 5 μm ($\equiv D_x^{\text{max}}$) for the marginally confining 12 μm band. In contrast, D_x^{max} = 7.5 μm on the 6 μm band because of increased confinement and coalescence into single droplets. $D_x^{\text{max}} >$ 6 μm also implies that the three phase contact line crosses over to the adjacent $-\text{CH}_3$ bands. Further confinement (1.5 μm) results in a multimodal distribution representing discrete events of bridging across multiple bands. Observe that there are no droplets of 1.5 μm size (since $\Lambda_{\text{isotropic}} =$ 4.2 μm $> 1.5 \ \mu$m).

     Macros were developed to identify droplet centers of mass and section profiles along the x- and y-axes. Analysis of databases of maximal slopes for 30–60 droplets per scan was performed to give distributions of contact angles. These distributions are independent of AFM scan direction. Large droplet sizes (μm) and low contact angles ($<10°$) preclude artifacts due to AFM tip geometry. Notably, these polymeric systems indeed show a fairly wide distribution of contact angles so that measurements for individual droplets are not generally representative. The contact angles measured also vary around the contact line of each droplet, requiring careful discrimination between the x-directional and y-directional contact angles. The x-

     (36) 1-D coalescence dictates that the pinned advancing front (x-axis) be discriminated from the lower receding angles (y-axis).

directional contact angle distributions are shown in Figure 9c. The 12 μm bands have droplet contact angles of $\theta_x = 8°$ and a pseudo-contact-angle $\theta_x = 6°$, corresponding to the saddle between two coalescing droplets. The 6 μm band, in contrast, has a sharp monomodal distribution with $\theta_x = 8°$ in a confined "channel state".[18] Distributions along the *y*-axis are similar (not shown) but, for the confining dimensions (<6 μm), lag behind those along the *x*-axis by a degree. The droplet coalescence mechanism would dictate that the "pinned" advancing front (*x*-axis) is discriminated from the lower receding contact angles along the *y*-axis. The distribution of θ_x on the 1.5 μm band has a range of *quantized* values from 3° to 10°. (Quantization of θ_x on chemical patterns was predicted by Lenz et al.,[18] but the 1-D three-phase equilibrium model is distinct from the 2-D PS droplet dynamics discussed above.) The contact angles reflect the morphological evolution with confining pattern dimensions, with distributions that go from bimodal for the 15−12 μm doublet state to monomodal (9−6 μm coalescence) and to the quantized multimodal bridging morphology. The lowest angles represent relaxed droplets on bridging while the highest represent high aspect ratio ellipsoidal drops. The highest contact angle ($\theta_x \approx 10°$) is higher than that on either the −CH$_3$ ($\theta_x = 8.3°$) or −COOH ($\theta_x = 7°$) region because of chemical potential induced pressure from nonwetting to the wetting regions.[17,29] (Young's law is not valid for confined droplets, as predicted.[18]) Droplets get "pinned" to the pattern dimension and then distort with further coalescence along the stripes. Bridging then occurs in discrete energetic steps. The crossover may be defined as a critical angle ($\theta_x \approx 10°$).

4. Conclusions

Pattern directed dewetting provides a powerful means of controlling the structure of polymer films over large areas. The regulation of the characteristic wavelength of the co-continuous patterns along both the axes with substrate pattern period demonstrates the control of the dewetting process by an imposed chemical field. The coupling of the dewetting patterns to the pattern scale and frequency at a relatively early stage influences the evolution to the final dewet morphology. We find that droplet arrays follow substrate patterns when the pattern size is comparable to the scale of the dewetting instability, as found in simulations.[17] Though this commensurability of scale may be needed for ideal pattern recognition, we confirm the presence of upper and lower cutoff scales that define morphological transitions from the "doublet" to the "channel" and then to the heterogeneous morphology. The quasi-1-D nature of droplet coarsening on stripes leads to interesting features: formation of droplet arrays, confinement and shape distortion, bridging transitions, and quantization of droplet size and contact angles.[18]

Appendix. Theoretical Estimate of Film Thickness for Onset of Spinodal Dewetting

The prediction of the thickness for the onset of spinodal instability ($\phi''(h) < 0$, $\phi(h) > 0$) requires estimation of the

metastable interfacial potential profile and an effective Hamaker constant ($A_{substrate}$) for an "air/PS/substrate" system.[37] A simple additive model for a "bulk-Au/SAM/PS/air" two-interface system by Seeman et al.[27] projects the van der Waals interfacial potential to be given by $\varphi(h)_{vdw} = -A_{SAM}/[12\pi h^2] + (A_{SAM} - A_{Au})/[12\pi(h + d)^2]$. The opposing signs of the Hamaker constants ($A_{SAM} = 8.3 \times 10^{-21}$ J; $A_{Au} = -6.7 \times 10^{-20}$ J) in the model suggest a metastable PS film which will spinodally dewet at $h = 3.7$ nm. The Hamaker constants here are evaluated for two macroscopic phases 1 and 2 interacting across a medium 3 by integration of the expression,

$$A = \frac{3}{4}kT\left(\frac{\epsilon_1 - \epsilon_3}{\epsilon_1 + \epsilon_3}\right)\left(\frac{\epsilon_2 - \epsilon_3}{\epsilon_2 + \epsilon_3}\right) + \frac{3h}{4\pi}kT\int_{\nu_1}^{\infty}\left(\frac{\epsilon_1(i\nu) - \epsilon_3(i\nu)}{\epsilon_1(i\nu) + \epsilon_3(i\nu)}\right)\left(\frac{\epsilon_2(i\nu) - \epsilon_3(i\nu)}{\epsilon_2(i\nu) + \epsilon_3(i\nu)}\right) d\nu$$

where the complex frequency response for a metallic Au film, $\epsilon_2(i\nu) = 1 + \nu_{2,e}^2/\nu^2$, is treated distinctly from $\epsilon_3(i\nu) = 1 + (n_3^2 - 1)/(1 + \nu_{3,e}^2/\nu^2)$ for the dielectric media. Experimental observations by Kane et al., however, have measured a substantial reduction in the dispersion interaction between Au surfaces following derivatization with 11-unmercatodecanoic acid.[38] The Lifshitz−van der Waals potential for a complex multilayered system of SAMs on thin Au films has also been shown by Ederth to be sensitive to the thickness of the Au layer and the SAM height.[39] Though the recent computations by Ederth[39] evaluate the van der Waals potential for a symmetric case of SiO/Ti/Au/SAM/H$_2$O half-space, the strong attenuation of the interactions suggests careful evaluation of the calculations for our nonsymmetric multilayer case with thin metallic films. On the basis of Lifshitz's theory and the treatment of Mahanty and Ninham[40] for many-layered systems, the Ederth continuum model accounts for thickness and retardation effects for each layer, while accounting for the dielectric response at all imaginary frequencies for each material. Notably, the resulting nonmonotonic "Hamaker functions" obtained from this analysis indicate that the interfacial potential may not be approximated by a simple additive potential model.[27,39] Thus, the 3.7 nm thickness may be an underestimate for spinodal instability. Direct experimental measurement of the van der Waal interactions and the optical properties of each layer is essential for accurate predictive models of interfacial interactions of multilayer systems. Accounting for attenuation in the resulting "Hamaker functions"[17] for thin Au films and retardation in a multilayer Si/Au-(100 Å)/SAM/PS/air system, we may estimate spinodal instability ($\phi'' < 0$) for $h < 20$ nm. Significantly, Kargupta et al.[29] have also pointed to a shift in the interfacial potential profiles on chemically heterogeneous substrates, suggesting a complex scenario that the films may be spinodally unstable at higher initial thickness in the presence of a chemical potential field.

(37) Israelachvili, J. N. *Intermolecular and Surface Forces*, 2nd ed.; Academic Press Inc.: San Diego, CA, 1992.
(38) Kane, V.; Mulvaney, P. *Langmuir* **1998**, *14*, 3303−3311.
(39) Ederth, T. *Langmuir* **2001**, *17*, 3329−3340.
(40) Mahanty, J.; Ninham, B. W. *Dispersion Forces*; Academic Press Inc.: New York, 1976.